

Tumor Budding T-cell Graphs: Assessing the Need for Resection in pT1 Colorectal Cancer Patients

Linda Studer^{1,2,3}

LINDA.STUDER@UNIFR.CH

¹ Document, Image and Video Analysis Research Group, University of Fribourg, Switzerland

² iCoSys, University of Applied Sciences and Arts Western Switzerland, Fribourg, Switzerland

³ Institute of Tissue Medicine and Pathology, University of Bern, Switzerland

John-Melle Bokhorst⁴

JOHN-MELLE.BOKHORST@RADBOUDUMC.NL

⁴ Department of Pathology, Radboudumc, Nijmegen, Netherlands

Iris Nagtegaal⁴

IRIS.NAGTEGAAL@RADBOUDUMC.NL

Inti Zlobec³

INTI.ZLOBEC@UNIBE.CH

Heather Dawson³

HEATHER.DAWSON@UNIBE.CH

Andreas Fischer^{1,2}

ANDREAS.FISCHER@HEFR.CH

Editors: Accepted for publication at MIDL 2023

Abstract

Colon resection is often the treatment of choice for colorectal cancer (CRC) patients. However, especially for minimally invasive cancer, such as pT1, simply removing the polyps may be enough to stop cancer progression. Different histopathological risk factors such as tumor grade and invasion depth currently form the basis for the need for colon resection in pT1 CRC patients. Here, we investigate two additional risk factors, tumor budding and lymphocyte infiltration at the invasive front, which are known to be clinically relevant. We capture the spatial layout of tumor buds and T-cells and use graph-based deep learning to investigate them as potential risk predictors. Our pT1 Hotspot Tumor Budding T-cell Graph (pT1-HBTG) dataset consists of 626 tumor budding hotspots from 575 patients. We propose and compare three different graph structures, as well as combinations of the node labels. The best-performing Graph Neural Network architecture is able to increase specificity by 20% compared to the currently recommended risk stratification based on histopathological risk factors, without losing any sensitivity. We believe that using a graph-based analysis can help to assist pathologists in making risk assessments for pT1 CRC patients, and thus decrease the number of patients undergoing potentially unnecessary surgery. Both the code and dataset are made publicly available.

Keywords: Digital Pathology, Graph Neural Networks, Colorectal Cancer

1. Introduction

Thanks to screening programs becoming more common, colorectal cancer (CRC) is getting diagnosed in earlier, and more easily treatable stages. pT1 is such a form of early CRC, only invading the submucosa, but not yet the muscle layer. Thus, defining appropriate treatment guidelines is of high importance. Even though these cancers are minimally invasive, they can still cause lymph node metastasis, which puts patients at risk for distant metastasis (Burt et al., 2010; Argilés et al., 2020). That, however, cannot be assessed just from the polypectomy, but only after surgical colon resection (also referred to as a colectomy).

Among pT1 CRC patients, less than 15% actually have metastasis present in lymph nodes at the time of diagnosis (Nivatvongs et al., 1991; Kobayashi et al., 2012; Dykstra et al., 2021). Cancer registry data¹ in Bern, Switzerland from 2014 show that 55% of all pT1 CRC patients nonetheless underwent a colectomy. (Zwager et al., 2022) find an even higher disparity, from the 70%–80% patients considered as high risk, more than 90% are lymph node negative. This is due to current clinical guidelines (Bosch et al., 2013; Argilés et al., 2020) commonly recommending that patients should undergo surgery in the presence of just one unfavorable histological risk factor. Hence, improving this risk assessment has a high potential to reduce overtreatment and potential clinical complications (Vermeer et al., 2019; Zwager et al., 2022).

Deep learning has provided solutions to a variety of challenges in pathology in recent years (Echle et al., 2021; Gurcan et al., 2009), such as tissue segmentation (Abbet et al., 2022), survival analysis (Bychkov et al., 2018; Abbet et al., 2020), and predicting lymph node metastasis (Kiehl et al., 2021; Brockmoeller et al., 2022; Khan et al., 2023). Lately, especially the combination of deep learning with spatial analysis has become of high interest (Jaume et al., 2021; Ahmedt-Aristizabal et al., 2021; Pati et al., 2022). Graph-based representations allow us to capture the spatial layout of the tissue and cells of interest and map their interactions in a very concise way. Thus, they make it possible to focus the deep learning algorithm on entities with known histopathological and clinical importance.

Two such factors that are known to play an important role in CRC are tumor budding and CD8+ lymphocytes (also known as cytotoxic T-cells), especially at the invasive front (Lugli et al., 2009). Tumor budding is a well-established prognostic factor in CRC (Lugli et al., 2017; Studer et al., 2021a). Several studies have also highlighted the prognostic power of T-cell scoring (Alwers et al., 2022). Most studies actually investigate the T-cell scoring in relation to tumor budding (Dawson et al., 2020; Nearchou et al., 2021; Lugli et al., 2009; Nearchou et al., 2019; Studer et al., 2022). However, so far the analysis has been limited to creating statistical scores, based on the ratio of counts in areas or within a radius, and other spatial statistics, and are performed on multi-stage cohorts.

To our knowledge, this is the first work exploring the interaction between tumor buds and T-cells using a graph-based approach. Another contribution is our investigation of different graph representations and making the dataset publicly available. Additionally, we aim to address a question of high clinical importance, as risk assessment of polypectomy specimens will only become more important in the future.

The paper is structured as follows: Section 2 describes the used Graph Neural Networks (GNNs) methods, Section 3 introduces the dataset, and Section 4 provides details on the experimental setup and presents the results. Finally, Section 5 summarizes our findings.

2. Graph Neural Networks

With the introduction of GNNs, the field of deep learning has been expanded into the domain of graph-based analysis. Mathematically, a graph G is defined as a tuple of (N, E, α, β) , where N denotes a finite set of nodes (or vertices), and E a set of edges, which are inserted according to a specified edge insertion function, and α and β are the node and edge labeling functions, respectively.

1. <https://www.krebsregister.unibe.ch>

For classification tasks, GNNs architectures can be divided into two phases, a message-passing (MP) and a read-out phase. During the MP phase, information is exchanged between connected nodes, and then aggregated to update their hidden state:

$$\mathbf{a}_i^{k+1} = \text{AGGREGATE}_{j \in \mathcal{N}(i)}(\mathbf{x}_i^k, \mathbf{x}_j^k, \mathbf{e}_{ij}^k) \quad (1)$$

$$\mathbf{x}_i^{k+1} = \text{UPDATE}(\mathbf{x}_i^k, \mathbf{a}_i^{k+1}), \quad (2)$$

where $\mathcal{N}(i)$ denotes the neighbouring nodes of node i , x_i the feature vector of node i , e_{ij} the edge feature vector between node i and j . In the first round (or layer) of MP, the hidden node state is the node feature vector of the input graph. By performing k rounds (or layers) of MP, the aggregation range is extended to the k -hop neighborhood.

Over the years, many different MP functions have been introduced, however, the performance of a GNN model is highly dependent on the graph type and the right choice is not trivial (Thomas et al., 2022; You et al., 2020). We use and compare three of the most commonly used ones for graph classification, namely GraphSAGE, GIN, and GATv2. They are all based on graph convolution, more details are provided in Appendix B.

In order to perform graph classification, the information of all hidden node states is aggregated and passed to the classification header, which is often a multi-layer perceptron (MLP). This is referred to as the read-out phase:

$$\mathbf{v}_G = \text{READOUT}(\mathbf{x}_i^K | i \in G). \quad (3)$$

where \mathbf{x}_i^K is the node state after the last MP round. However, it has been shown to be beneficial to also consider the intermediate representations, i.e. performing a read-out after each layer. These skip connections were introduced by (Xu et al., 2018b) and termed Jumping Knowledge (JK). The different read-out vectors can e.g. be concatenated such as $\mathbf{v}_G = \mathbf{v}^1 \| \dots \| \mathbf{v}^K$. The first part of Figure 1 gives an overview of the GNN architecture.

3. pT1 Hotspot Tumor Budding T-cell Graph (pT1-HBTG) Dataset

The graph creation workflow is depicted in Figure 1. Figure 2 shows an example image for each graph representation and class. The pT1-HBTG dataset is available open-source², additional details on the dataset and more example images can be found in Appendix C.

3.1. pT1 Patient Cohort

Our pT1 cohort consists of patients that, after the polypectomy, either (A) underwent resection, and thus have a known lymph node status, or (B) have at least 36 months of follow-up information about local/distant recurrence. We categorize the patients as either high- or low-risk, according to the clinical question of whether, in retrospect, they required the colectomy. Patients (A) without lymph node metastasis (N0) and patients (B) without recurrence are considered low-risk. Thus, patients (A) with lymph node metastasis (N+) and patients (B) with a recurrence are grouped into the high-risk class.

In total, we have 626 whole slide images (WSIs) of polyps from 575 pT1 CRC patients collected from eight different pathology institutes and selected by expert pathologists. The

2. <https://zenodo.org/record/7867085>

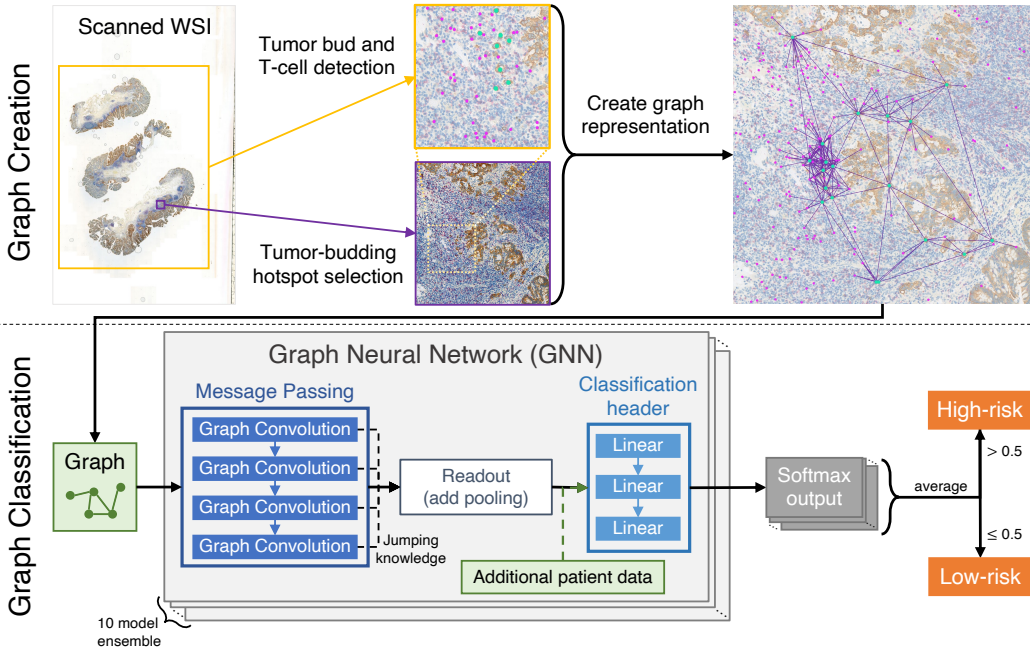


Figure 1: Schematic overview of the framework. To build the graph, tumor buds and T-cells are automatically detected using CNNs, and the tumor budding hotspot is selected by a pathologist. All detected objects within it are then used as nodes to build the graph representation (tumor bud detections are highlighted in green, and T-cells in pink). The example shown here is the *Delaunay-Star* edge configuration. The graph classification GNN consists of a message passing phase, followed by a readout phase, and a classification MLP. An ensemble of 10 models is used to make the risk classification, based on the averaged softmax output.

WSIs are double-stained for CD8-AE1/AE3 using immunohistochemistry (AE1-AE3 pan-cytokeratin for the tumor, and CD8 for the cytotoxic T-cells). They are digitized using a Pannoramic 250 scanner at $0.243\mu\text{m}/\text{pixel}$. The class distribution is unbalanced, with 541 versus 85 for the low-risk and high-risk groups, respectively.

3.2. Graph Representations

The pT1-HBTGs represent the tumor budding hotspot of a slide according to the IT-BCC (Lugli et al., 2017) recommendations (area of highest budding at the invasive front, 0.785mm^2), selected by an expert pathologist. As introduced in section 2, a graph consists of *nodes* and *edges*, which are inserted according to a specified edge insertion function. Both nodes and edges can have additional information attached to them, also referred to as *labels*. The pipeline for graph creation is available on GitHub³.

3. <https://github.com/digitalpathologybern/BT-graph-creation>

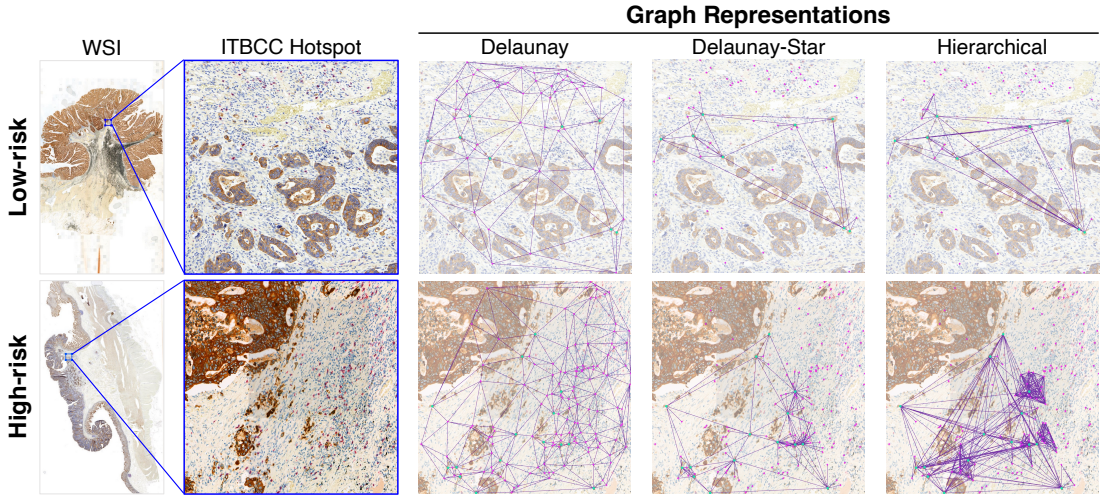


Figure 2: Example graph representations for a low- and a high-risk patient. The nodes are color-coded based on the *type* node label, tumor buds in green and T-cells in pink. The blue rectangle on the WSI shows the annotation of the ITBCC hotspot.

3.2.1. NODE DETECTION AND NODE LABELING

Since our graphs map the interaction of tumor buds with T-cells, they build the nodes of our graphs. T-cells are single cells, whereas a tumor bud is defined as a cluster of 1-4 tumor cells. The tumor bud detection is performed using a student-teacher CNN (Bokhorst et al., 2022) model, which is available on Grand Challenge⁴. The algorithm used for the T-cells is based on U-Net, with additional post-processing (Gaussian filtering and regional maxima detection) (Swiderska-Chadaj et al., 2019). Color deconvolution is performed as a pre-processing step as the algorithm is trained on single-stain immunohistochemistry (IHC). The quality of the output was manually reviewed by an expert pathologist on a subset, with a precision of 89.9% and recall of 93.0% (Studer et al., 2020).

We define three different types of node features. First, the *type* of the node, i.e. tumor bud or T-cell, which is one-hot encoded. Second, we use the *coordinates* of the node, normalized to the center of the hotspot using zero centering: $x' = x - \bar{x}$. Third, we compute the *embedding vector* of crops (200×200 pixels centered on the node coordinates) using the ImageNet (Deng et al., 2009) pre-trained DINO model (Caron et al., 2021). Using the ViT-16 backbone, we get a feature vector of size 384.

3.2.2. EDGE INSERTION AND EDGE LABELLING

As an edge label, we use the distance between the nodes in μm . We define three different edge insertion functions. As a baseline, we use the *Delaunay* triangulation (Delaunay and Sphrevide, 1934) (without distinguishing between the two node types), which is very commonly used in histopathology, especially for cell graphs (Sharma et al., 2015). We only consider two cell (cluster) types as nodes and not all cells, as we are especially interested

4. <https://grand-challenge.org/algorithms/colon-budding-in-ihc/>

Table 1: Options for the experimental setups. In total, this results in 144 setups for all combinations of graph configurations, node labels, message passing functions, and with/without JK and additional clinical information.

Graph Options	Edge Configuration	Delaunay, Delaunay-Star, Hierarchical
	Node Labels	Type (tumor bud or T-cell), coordinates, ViT-16 embedding
GNN	MP Functions	GraphSAGE, GIN, GATv2
	Jumping Knowledge (JK)	With and without
Additional Data	Clinical Information (SGG Criteria)	With and without

in the interaction of the T-cells within close proximity of the tumor buds. Thus, *Delaunay* triangulation might not be the best way to capture this spatial relationship, we define two more edge insertion functions. Firstly, we propose a *Hierarchical* representation, where all T-cells nodes are connected to their closest tumor bud node, with a cut-off of $100\mu\text{m}$. Then, all T-cell nodes connected to the same tumor bud are fully-connected. Lastly, the tumor bud nodes are fully-connected as well. Secondly, we define the *Delaunay-Star* representation, the tumor bud nodes are connected using Delaunay triangulation, and the T-cell nodes are connected to all tumor bud nodes within a radius of $100\mu\text{m}$.

4. Experimental Evaluation

In this section, we provide the details of the experimental setups and present the results of the best-performing ones. A schematic overview of the whole experimental framework can be found in Figure 1. As a baseline, we use the risk assessment guidelines defined by the Swiss Society of Gastroenterologists (SGG) (Dieter, 2022), which define the current treatment recommendations for pT1 polyps for Swiss pathologists. For more details on the SGG criteria see Appendix A. Because the dataset is unbalanced, we use the following metrics to assess the performance: Average F1Score (average of per-class score), the True Negative Rate (TNR), and the True Positive Rate (TPR). The TNR is the recall for the low-risk class and is also called specificity or selectivity. The TPR is the recall for the high-risk group, also known as sensitivity.

4.1. Experimental Setup

We use a 5-fold cross-validation (CV) setup. The data is split so that patients do not overlap, and the distribution between the two classes is roughly the same in each fold (see Table D5). The evaluation is done per patient. If there are multiple graphs per patient, the classification is based on $\max(\text{softmax}(\mathbf{z}_1), \dots, \text{softmax}(\mathbf{z}_n))$ with z being the output of the classification MLP, and n the total number of graphs. Each experimental setup is run 5 times with a different seed. An ensemble of these 5 models is used for the risk classification,

Table 2: Best results for all node label and graph configuration combinations are presented here (5-model ensemble, average and standard deviation over 5-fold CV). For the complete result tables see Appendix E. As a baseline, we report the classification based on the guidelines by the SGG (see Figure 3). True Negative Rate (TNR): recall for the low-risk group. True Positive Rate (TPR): recall for the high-risk group). The top three are indicated in bold.

Node Label	Edge Config	GNN	Clin. Info	Average F1Score (%)	TNR (%)	TPR (%)
Type	Delaunay	GraphSAGE-JK	Yes	35.2 ± 3.3	31.4 ± 4.7	88.3 ± 5.1
	Delaunay-Star	GraphSAGE-JK	Yes	39.5 ± 8.1	40.2 ± 13.1	79.9 ± 13.5
	Hierarchical	GIN-JK	No	30.4 ± 14.4	27.9 ± 20.7	83.7 ± 13.5
Type Coord.	Delaunay	GIN-JK	No	27.1 ± 11.2	24.1 ± 22.1	83.0 ± 21.4
	Delaunay-Star	GraphSAGE-JK	Yes	37.2 ± 6.6	35.9 ± 8.2	80.2 ± 5.6
	Hierarchical	GraphSAGE	Yes	33.5 ± 4.9	30.0 ± 8.4	84.4 ± 14.3
Type ViT-16.	Delaunay	GATv2	Yes	36.3 ± 8.7	32.6 ± 10.8	90.5 ± 9.6
	Delaunay-Stars	GIN-JK	Yes	40.9 ± 13.2	41.5 ± 18.6	84.2 ± 6.1
	Hierarchical	GATv2	Yes	41.1 ± 12.7	40.7 ± 15.6	84.8 ± 8.4
Type	Delaunay	GIN-JK	No	35.2 ± 10.7	32.9 ± 14.9	83.3 ± 9.8
Coord.	Delaunay-Star	GraphSAGE-JK	Yes	39.7 ± 4.2	38.4 ± 4.8	85.7 ± 9.9
ViT-16	Hierarchical	GraphSAGE-JK	Yes	41.9 ± 5.4	42.5 ± 8.9	84.0 ± 8.2
SGG Criteria Classification				28.2 ± 4.4	22.2 ± 4.3	85.0 ± 7.6

by taking the average of the softmax output. This lets us take the certainty of each model into account.

Table 1 shows the different options for the experimental setups (total of 144 experiments). The additional clinical information used as input for the classification header is based on the SGG criteria: lymphovascular invasion yes/no (one hot encoded), tumor grade (1-3), $\log_{10}(\text{number of tumor buds})$ and $\log_{10}(\text{invasion depth})$ in mm. The numerical variables are \log_{10} transformed to be near normal distributed. The implementation details can be found in Appendix D and the code is available on GitHub⁵.

4.2. Results and Discussion

Table 2 shows the best results for each graph structure and node label combination, we consider the top-3 performing models for each graph structure and node label combination in terms of average F1Score and average Recall ($\frac{\text{TNR}+\text{TPR}}{2}$) and select the one with the highest TPR among them (disregarding models with a TNR below the baseline). The complete result (with additional metrics) can be found in Appendix E. If the main goal is to prevent unnecessary surgeries, a high TNR is important. If we choose the model with the

5. <https://github.com/digitalpathologybern/pT1-HBTG-MIDL2023>

highest average F1Score, we select a model that shows an increased performance for both the TNR and TPR compared to the baseline. For both of these metrics, the GraphSAGE-JK architecture trained on the *Hierarchical-Type-Coordinate-ViT16* graphs, and using the additional clinical information, shows the best performance. If not missing any high-risk patient is of high importance, and a moderate improvement in the TNR is acceptable, the GATv2 trained on the *Delaunay-Type-ViT16* graphs, and using the additional clinical information, should be considered. It is notable that the GraphSAGE-JK model trained on the *Delaunay-Type* graphs (using the clinical data), the most simple representation, also performs well, and additionally has the lowest standard deviation. Ockham’s razor would thus suggest, that this model is preferred due to its simplicity. Since this representation does not use any image-based features, it also bypasses any bias that could be caused by the image data, e.g. staining variation.

As observed in (You et al., 2020), the architecture of the GNN depends heavily on the graph. We can see this here, in that different architectures perform best for different graph structures and node label combinations. However, using a variation of *Delaunay* triangulation to create graphs seems to be a generally good choice to perform spatial analysis in digital pathology, not only when using cell graphs. Interestingly, GraphSAGE shows good performance, even though it is the simplest MP function. This is likely because larger, and more complex models are more prone to overfitting, especially on small datasets. We also observe that some combinations seem more prone to overfitting, showing a high variance between the CV-folds, especially the experiments using the GIN MP function. Using JK seems to be preferred for both GraphSAGE and GIN, but not for GATv2.

5. Conclusion

In this study, we explore the potential of analyzing the interaction between the tumor and the immune system at the invasive front using graph-based deep learning for risk assessment of pT1 CRC patients. We introduce our publicly available pT1 Hotspot Tumor Budding T-cell Graph (pT1-HBTG) dataset and investigate the predictive power of different graph representations (edge insertion functions and node labels). Using GNN models, especially when combined with known histopathological risk factors, we are able to outperform the risk stratification according to current treatment recommendations and decrease the number of falsely identified high-risk patients by 20%, without a decrease in sensitivity. Creating the graphs is agnostic to the way lymphocytes and tumor buds are detected and thus can be adapted to the available image processing methods. For future work, we hope to validate our proposed methods on an external cohort and extend our findings to other cancer patient groups of interest, such as stage II CRC.

Acknowledgments

The work presented here is supported by the Rising Tide Foundation with grant number CCR-18-130. Many thanks also go to my collaborators who helped collect the patient cohort, namely Prof. Dr. med. Gerhard Seitz (Klinikum Bamberg, Germany), Prof. Dr. med. M. Vieth (Klinikum Bayreuth, Germany), Prof. Dr. med. Gieri Cathomas (formerly Kantonsspital Baselland, Switzerland) and Scott&White Healthcare (Temple, USA).

References

- Christian Abbet, Inti Zlobec, Behzad Bozorgtabar, and Jean-Philippe Thiran. Divide-and-rule: self-supervised learning for survival analysis in colorectal cancer. In *International Conference on Medical Image Computing and Computer-Assisted Intervention*, pages 480–489. Springer, 2020.
- Christian Abbet, Linda Studer, Andreas Fischer, Heather Dawson, Inti Zlobec, Behzad Bozorgtabar, and Jean-Philippe Thiran. Self-rule to multi-adapt: Generalized multi-source feature learning using unsupervised domain adaptation for colorectal cancer tissue detection. *Medical image analysis*, 79:102473, 2022.
- David Ahmedt-Aristizabal, Mohammad Ali Armin, Simon Denman, Clinton Fookes, and Lars Petersson. A survey on graph-based deep learning for computational histopathology. *Computerized Medical Imaging and Graphics*, page 102027, 2021.
- Elizabeth Alwers, Jakob N Kather, Matthias Kloos, Alexander Brobeil, Katrin E Tagscherer, Wilfried Roth, Amelie Echle, Efrat L Amitay, Jenny Chang-Claude, Hermann Brenner, et al. Validation of the prognostic value of cd3 and cd8 cell densities analogous to the immunoscore® by stage and location of colorectal cancer: an independent patient cohort study. *The Journal of Pathology: Clinical Research*, 2022.
- G Argilés, J Tabernero, R Labianca, D Hochhauser, R Salazar, T Iveson, P Laurent-Puig, P Quirke, T Yoshino, J Taieb, et al. Localised colon cancer: Esso clinical practice guidelines for diagnosis, treatment and follow-up. *Annals of Oncology*, 31(10):1291–1305, 2020.
- John-Melle Bokhorst, Iris D Nagtegaal, Inti Zlobec, Heather Dawson, Kieran Sheahan, Femke Simmer, Richard Kirsch, Michael Vieth, Alessandro Lugli, Jeroen Laak, et al. Semi-supervised learning to automate tumor bud detection in cytokeratin-stained whole-slide images of colorectal cancer. *preprint*, 2022.
- Steven L Bosch, Steven Teerenstra, Johannes HW de Wilt, Chris Cunningham, and Iris D Nagtegaal. Predicting lymph node metastasis in pt1 colorectal cancer: a systematic review of risk factors providing rationale for therapy decisions. *Endoscopy*, 45(10):827–841, 2013.
- Scarlet Brockmoeller, Amelie Echle, Narmin Ghaffari Laleh, Susanne Eiholm, Marie Louise Malmstrøm, Tine Plato Kuhlmann, Katarina Levic, Heike Irmgard Grabsch, Nicholas P West, Oliver Lester Saldanha, et al. Deep learning identifies inflamed fat as a risk factor for lymph node metastasis in early colorectal cancer. *The Journal of pathology*, 256(3):269–281, 2022.
- Shaked Brody, Uri Alon, and Eran Yahav. How attentive are graph attention networks? *arXiv preprint arXiv:2105.14491*, 2021.
- Randall W Burt, James S Barthel, Kelli Bullard Dunn, Donald S David, Ernesto Drelichman, James M Ford, Francis M Giardiello, Stephen B Gruber, Amy L Halverson, Stanley R Hamilton, et al. Nccn clinical practice guidelines in oncology. colorectal cancer

screening. *Journal of the National Comprehensive Cancer Network: JNCCN*, 8(1):8–61, 2010.

Dmitrii Bychkov, Nina Linder, Riku Turkki, Stig Nordling, Panu E Kovanen, Clare Verrill, Margarita Walliander, Mikael Lundin, Caj Haglund, and Johan Lundin. Deep learning based tissue analysis predicts outcome in colorectal cancer. *Scientific reports*, 8(1):1–11, 2018.

Tianle Cai, Shengjie Luo, Keyulu Xu, Di He, Tie-yan Liu, and Liwei Wang. Graphnorm: A principled approach to accelerating graph neural network training. In *International Conference on Machine Learning*, pages 1204–1215. PMLR, 2021.

Mathilde Caron, Hugo Touvron, Ishan Misra, Hervé Jégou, Julien Mairal, Piotr Bojanowski, and Armand Joulin. Emerging properties in self-supervised vision transformers. In *Proceedings of the IEEE/CVF International Conference on Computer Vision*, pages 9650–9660, 2021.

Heather Dawson, Lucine Christe, Micha Eichmann, Stefan Reinhard, Inti Zlobec, Annika Blank, and Alessandro Lugli. Tumour budding/t cell infiltrates in colorectal cancer: proposal of a novel combined score. *Histopathology*, 76(4):572–580, 2020.

B Delaunay and Surla Spherevide. A la memoire de georges voronoi. *Bulletin de l'Académie des Sciences de l'URSS, Classe des sciences mathématiques et naturelles*, 6:793–800, 1934.

Jia Deng, Wei Dong, Richard Socher, Li-Jia Li, Kai Li, and Li Fei-Fei. Imagenet: A large-scale hierarchical image database. In *2009 IEEE conference on computer vision and pattern recognition*, pages 248–255. IEEE, 2009.

Koeberle Dieter. Nachsorge nach koloskopischer polypektomie und therapie des kolorektalen karzinoms. *Swiss Medical Forum*, 2022.

Mark A Dykstra, Tamara I Gimon, Paul E Ronksley, W Donald Buie, and Anthony R MacLean. Classic and novel histopathologic risk factors for lymph node metastasis in t1 colorectal cancer: a systematic review and meta-analysis. *Diseases of the Colon & Rectum*, 64(9):1139–1150, 2021.

Amelie Echle, Niklas Timon Rindtorff, Titus Josef Brinker, Tom Luedde, Alexander Thomas Pearson, and Jakob Nikolas Kather. Deep learning in cancer pathology: a new generation of clinical biomarkers. *British journal of cancer*, 124(4):686–696, 2021.

Catarina Eloy and Sofia Campelos. What did we expected from porto's ecdp2020? *Journal of Pathology Informatics*, 11, 2020.

Matthias Fey and Jan E. Lenssen. Fast graph representation learning with PyTorch Geometric. In *ICLR Workshop on Representation Learning on Graphs and Manifolds*, 2019.

Metin N Gurcan, Laura E Boucheron, Ali Can, Anant Madabhushi, Nasir M Rajpoot, and Bulent Yener. Histopathological image analysis: A review. *IEEE reviews in biomedical engineering*, 2:147–171, 2009.

Will Hamilton, Zhitao Ying, and Jure Leskovec. Inductive representation learning on large graphs. *Advances in neural information processing systems*, 30, 2017.

Guillaume Jaume, Pushpak Pati, Valentin Anklin, Antonio Foncubierta, and Maria Gabrani. Histocartography: A toolkit for graph analytics in digital pathology. In *MICCAI Workshop on Computational Pathology*, pages 117–128. PMLR, 2021.

Amjad Khan, Nelleke Brouwer, Annika Blank, Felix Müller, Davide Soldini, Aurelia Noske, Elisabeth Gaus, Simone Brandt, Iris Nagtegaal, Heather Dawson, et al. Computer-assisted diagnosis of lymph node metastases in colorectal cancers using transfer learning with an ensemble model. *Modern Pathology*, page 100118, 2023.

Lennard Kiehl, Sara Kuntz, Julia Höhn, Tanja Jutzi, Eva Krieghoff-Henning, Jakob N Kather, Tim Holland-Letz, Annette Kopp-Schneider, Jenny Chang-Claude, Alexander Brobeil, et al. Deep learning can predict lymph node status directly from histology in colorectal cancer. *European Journal of Cancer*, 157:464–473, 2021.

Hirotoshi Kobayashi, Tetsuro Higuchi, Hiroyuki Uetake, Satoru Iida, Toshiaki Ishikawa, Megumi Ishiguro, and Kenichi Sugihara. Resection with en bloc removal of regional lymph node after endoscopic resection for t1 colorectal cancer. *Annals of surgical oncology*, 19(13):4161–4167, 2012.

A Lugli, E Karamitopoulou, I Panayiotides, P Karakitsos, G Rallis, G Peros, G Iezzi, G Spagnoli, M Bihl, L Terracciano, et al. Cd8+ lymphocytes/tumour-budding index: an independent prognostic factor representing a ‘pro-/anti-tumour’approach to tumour host interaction in colorectal cancer. *British journal of cancer*, 101(8):1382–1392, 2009.

Alessandro Lugli, Richard Kirsch, Yoichi Ajioka, Fred Bosman, Gieri Cathomas, Heather Dawson, Hala El Zimaity, Jean-François Fléjou, Tine Plato Hansen, Arndt Hartmann, et al. Recommendations for reporting tumor budding in colorectal cancer based on the international tumor budding consensus conference (itbcc) 2016. *Modern pathology*, 30(9):1299–1311, 2017.

Andrew L Maas, Awni Y Hannun, Andrew Y Ng, et al. Rectifier nonlinearities improve neural network acoustic models. In *Proc. icml*, volume 30, page 3. Atlanta, Georgia, USA, 2013.

Ines P Nearchou, Kate Lillard, Christos G Gavriel, Hideki Ueno, David J Harrison, and Peter D Caie. Automated analysis of lymphocytic infiltration, tumor budding, and their spatial relationship improves prognostic accuracy in colorectal cancer automated image analysis in colorectal cancer prognosis. *Cancer immunology research*, 7(4):609–620, 2019.

Ines Panicou Nearchou, Daniel Alexander Soutar, Hideki Ueno, David James Harrison, Ognjen Arandjelovic, and Peter David Caie. A comparison of methods for studying the tumor microenvironment’s spatial heterogeneity in digital pathology specimens. *Journal of Pathology Informatics*, 12(1):6, 2021.

Santhat Nivatvongs, Arun Rojanasakul, Herbert M Reiman, Roger R Dozois, Bruce G Wolff, John H Pemberton, Robert W Beart, and Louis F Jacques. The risk of lymph

node metastasis in colorectal polyps with invasive adenocarcinoma. *Diseases of the colon & rectum*, 34(4):323–328, 1991.

Adam Paszke, Sam Gross, Francisco Massa, Adam Lerer, James Bradbury, Gregory Chanan, Trevor Killeen, Zeming Lin, Natalia Gimelshein, Luca Antiga, et al. Pytorch: An imperative style, high-performance deep learning library. *Advances in neural information processing systems*, 32, 2019.

Pushpak Pati, Guillaume Jaume, Antonio Foncubierta-Rodríguez, Florinda Feroce, Anna Maria Anniciello, Giosue Scognamiglio, Nadia Brancati, Maryse Fiche, Estelle Dubruc, Daniel Riccio, et al. Hierarchical graph representations in digital pathology. *Medical image analysis*, 75:102264, 2022.

Harshita Sharma, Norman Zerbe, Sebastian Lohmann, Klaus Kayser, Olaf Hellwich, and Peter Hufnagl. A review of graph-based methods for image analysis in digital histopathology. *Diagnostic pathology*, 1(1), 2015.

Linda Studer, John-Melle Bokhorst, Inti Zlobec, Alessandro Lugli, Andreas Fischer, Francesco Ciompi, Jeroen van der Laak, Iris Nagtegaal, and Heather Dawson. Validation of computer-assisted tumour-bud and t-cell detection in pt1 colorectal cancer. *Virchows Archiv, European Journal of Pathology*, 477(1):S37–S38, 2020.

Linda Studer, Annika Blank, John-Melle Bokhorst, Iris D Nagtegaal, Inti Zlobec, Alessandro Lugli, Andreas Fischer, and Heather Dawson. Taking tumour budding to the next frontier—a post international tumour budding consensus conference (itbcc) 2016 review. *Histopathology*, 78(4):476–484, 2021a.

Linda Studer, Jannis Wallau, Heather Dawson, Inti Zlobec, and Andreas Fischer. Classification of intestinal gland cell-graphs using graph neural networks. In *2020 25th International Conference on Pattern Recognition (ICPR)*, pages 3636–3643. IEEE, 2021b.

Linda Studer, John-Melle Bokhorst, Francesco Ciompi, Andreas Fischer, and Heather Dawson. Budding-t-cell score is a potential predictor for more aggressive treatment in pt1 colorectal cancers. In *European Congress of Digital Pathology (ECDP)*, 2022.

Zaneta Swiderska-Chadaj, Hans Pinckaers, Mart van Rijthoven, Maschenka Balkenhol, Margarita Melnikova, Oscar Geessink, Quirine Manson, Mark Sherman, Antonio Polonia, Jeremy Parry, et al. Learning to detect lymphocytes in immunohistochemistry with deep learning. *Medical image analysis*, 58:101547, 2019.

Christian Szegedy, Vincent Vanhoucke, Sergey Ioffe, Jon Shlens, and Zbigniew Wojna. Rethinking the inception architecture for computer vision. In *Proceedings of the IEEE conference on computer vision and pattern recognition*, pages 2818–2826, 2016.

Josephine M Thomas, Alice Moallemey-Oureh, Silvia Beddar-Wiesing, and Clara Holzhüter. Graph neural networks designed for different graph types: A survey. *arXiv preprint arXiv:2204.03080*, 2022.

NCA Vermeer, Y Backes, HS Snijders, E Bastiaannet, GJ Liefers, LMG Moons, CJH Van De Velde, and KCMJ Peeters. National cohort study on postoperative risks after surgery for submucosal invasive colorectal cancer. *BJS open*, 3(2):210–217, 2019.

Keyulu Xu, Weihua Hu, Jure Leskovec, and Stefanie Jegelka. How powerful are graph neural networks? *arXiv preprint arXiv:1810.00826*, 2018a.

Keyulu Xu, Chengtao Li, Yonglong Tian, Tomohiro Sonobe, Ken-ichi Kawarabayashi, and Stefanie Jegelka. Representation learning on graphs with jumping knowledge networks. In *International conference on machine learning*, pages 5453–5462. PMLR, 2018b.

Jiaxuan You, Zhitao Ying, and Jure Leskovec. Design space for graph neural networks. *Advances in Neural Information Processing Systems*, 33:17009–17021, 2020.

Liselotte W Zwager, Barbara AJ Bastiaansen, Nahid SM Montazeri, Roel Hompes, Valeria Barresi, Katsuro Ichimasa, Hiroshi Kawachi, Isidro Machado, Tadahiko Masaki, Weiqi Sheng, et al. Deep submucosal invasion is not an independent risk factor for lymph node metastasis in t1 colorectal cancer: a meta-analysis. *Gastroenterology*, 163(1):174–189, 2022.

Appendix A. Guidelines by the Swiss Society of Gastroenterologists

Figure 3 shows the risk assessment workflow recommended by the SGG for pT1 polyps. The criteria vary slightly between sessile and pedunculated polyps, as some of the scoring methods are different. In essence, however, they both cover tumor grade, infiltration depth, lymphovascular invasion, and tumor budding.

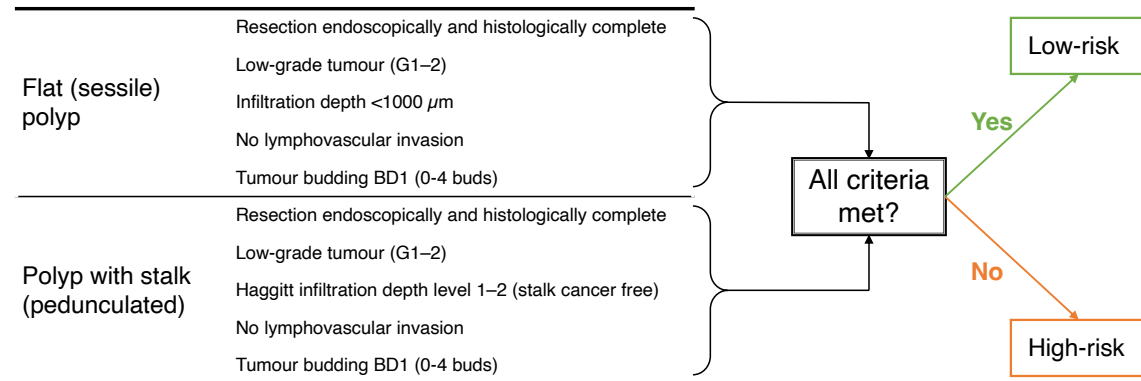


Figure 3: Prognostic classification criteria set forth by the SGG for risk assessment of pT1 polyp biopsies (Dieter, 2022). High-risk patients usually undergo colon resection, and low-risk patients follow a watch-and-wait strategy.

Appendix B. Message-passing Functions

This section provides the mathematical details of the used MP functions.

GraphSAGE (Hamilton et al., 2017) is one of the early proposed MP functions. The hidden node state is updated as follows, using the mean aggregator scheme:

$$\mathbf{x}_i^{k+1} = \mathbf{W}_1^k \mathbf{x}_i^k + \mathbf{W}_2^k \cdot \text{mean}_{j \in \mathcal{N}(i)} \mathbf{x}_j^k, \quad (4)$$

with $\mathcal{N}(i)$ here being a fixed number of uniformly drawn neighboring nodes.

GIN (graph isomorphism network) (Xu et al., 2018a) is designed to achieve maximum discriminative power. The hidden state is updated using an MLP, ϵ is either a learnable parameter or fixed between $[0, 1]$:

$$\mathbf{x}_i^{k+1} = \text{MLP} \left((1 + \epsilon) \cdot \mathbf{x}_i^k + \sum_{j \in \mathcal{N}(i)} \mathbf{x}_j^k \right) \quad (5)$$

vh GATv2 (Brody et al., 2021) incorporates an attention mechanism into the convolution, and is able to learn neighbor-specific weights, which can not only consider node but also edge features. The attention coefficients α_{ij} is defined as

$$\alpha_{ij} = \text{softmax}_j(\mathbf{a}^\top \text{LeakyReLU}(\mathbf{W} \cdot [\mathbf{x}_i \parallel \mathbf{x}_j \parallel \mathbf{e}_{i,j}]), \quad (6)$$

where \parallel denotes vector concatenation, and $\mathbf{a} \in \mathbb{R}^{2d'}$ and $\mathbf{W} \in \mathbb{R}^{d' \times d}$ are learned. The hidden representation of node i is thus updated as follows (σ is a non-linearity):

$$\mathbf{x}_i^{k+1} = \sigma \left(\sum_{j \in \mathcal{N}(i)} \alpha_{ij}^k \cdot \mathbf{W}^k \mathbf{x}_j^k \right). \quad (7)$$

Appendix C. Additional Details on the HBTG Dataset

Figure 4 provides more example images of the different graph types. See Table 4 for key statistics on the graphs in the different graph configuration datasets, and Table 3 for the clinical information within the high- and low-risk groups. A previous version of a subset of this dataset is described in (Eloy and Campelos, 2020). The code used to create the graph representations is available on GitHub⁶. The graph visualisation are created using a python tool that is also available on GitHub⁷

Appendix D. Additional Details on the Experimental Setup

The implementations are all done in PyTorch (Paszke et al., 2019), specifically, PyTorch Lightning, using the PyTorch Geometric (PyG) (Fey and Lenssen, 2019) library. Table 5 shows data distribution between the CV-folds, and Table 6 shows the number of parameters for each model.

We use a setup with four MP layers with 196 neurons each, and a three-layer MLP classification header, and between each layer, we add a dropout layer ($p = 0.3$). We also

6. <https://github.com/digitalpathologybern/BT-graph-creation>

7. https://github.com/DIVA-DIA/graph_visualisation

Table 3: Statistics on the pT1 patient cohort per group of interest in regards to the clinical information.

	Average Invasion Depth (mm)	Lymphovascular Invasion		Tumor Grade		
		Yes	No	1	2	3
Low-risk	5.00	79	434	140	333	40
High-risk	6.02	18	44	10	44	8
Total	5.11	97	478	150	377	48

Table 4: Graph configuration overview: median of graph feature in the pT1-HBTG. The low-risk group has a median number of 171 nodes (7 for tumor buds, 157 for T-cells), and the high-risk group 193 (16 tumor buds, 180 T-cells).

	Delaunay		Delaunay-Star		Hierarchical	
	Low-risk	High-risk	Low-risk	High-risk	Low-risk	High-risk
Edges	496	561	63	192	224	622
Connected Nodes	171	193	65	100	65	100
Isolated Nodes	0	0	106	93	106	93

employ the GraphNorm ([Cai et al., 2021](#)) normalization implemented in PyG between each MP layer to stabilize training. GraphNorm normalizes the node representations across all nodes per graph using a learnable shift α , which determines how much information to keep in the mean. We use the default $\alpha = 0.00001$.

After the read-out phase (global add-pooling), the graph embedding vector has a size of 196 or 784 neurons, as the output of all 4 MP layers are concatenated when using JK. The second MLP layer has double as many neurons, the last one again either 196 or 784. For the configuration, where additional patient data is used as input (concatenated with the read-out vector), an additional 5 neurons are added to the first layer. LeakyReLU ([Maas et al., 2013](#)) is used as an activation function (with default $\alpha = 0.01$).

For the MP functions, we use the implementations provided by PyG, with the following configurations:

- GraphSAGE: *SAGEConv*, no additional parameters need to be specified.
- GIN: *GINConv*, with a two-layer MLP (169 neurons, $\epsilon = 0$) using the LeakyReLU activation function and dropout ($p = 0.3$). Using an MLP and an $\epsilon = 0$ is suggested by ([Xu et al., 2018a](#)).
- GATv2: *GATv2Conv*, with a single attention header (default configuration).

The models are trained for 100 epochs (until convergence), with a batch size of 256, a learning rate and weight decay of 0.0001, and the *StepLR* learning rate scheduler (step-

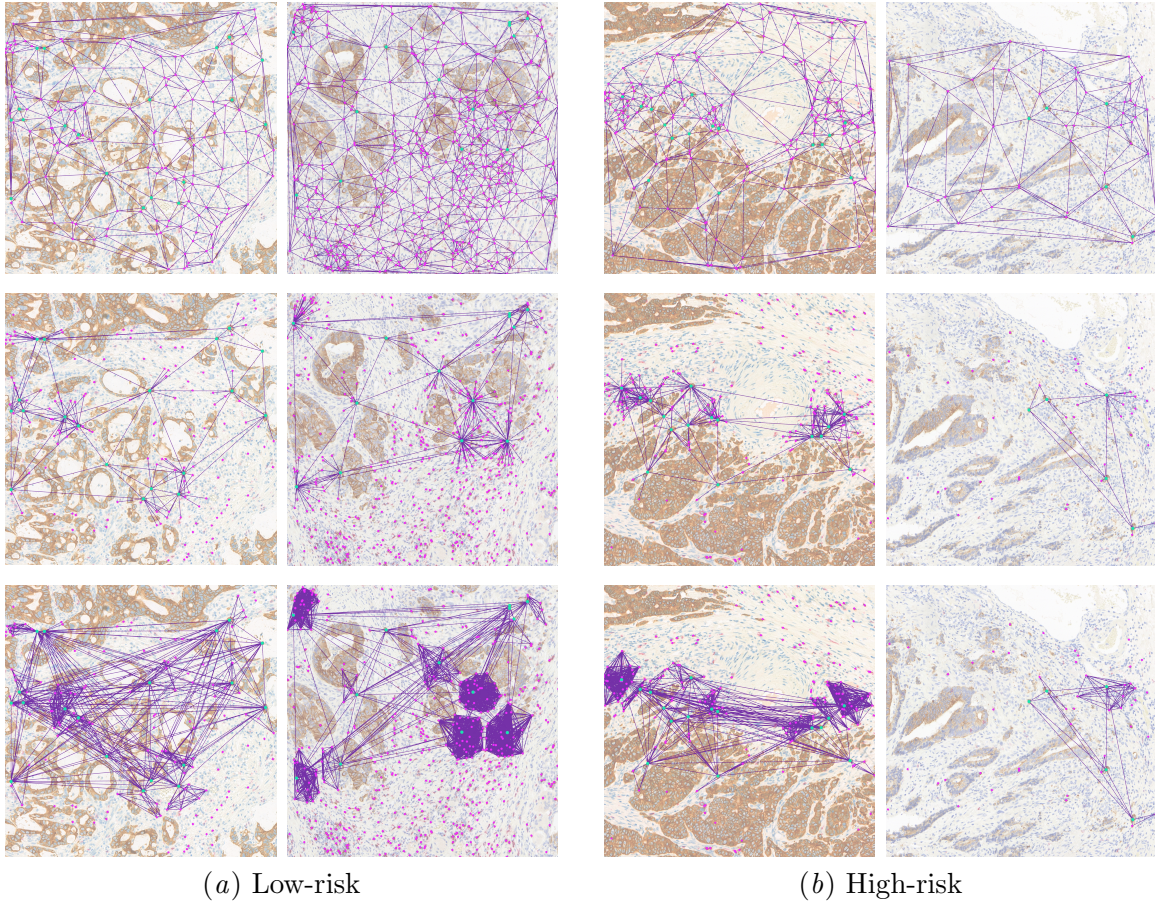


Figure 4: More examples from the pT1-HBTG datasets. The nodes are color-coded based on the *type* node label, tumor buds in green and T-cells in pink. The edges are in purple according to the edge insertion function described in Section 3.2.2: *Delaunay* (top), *Delaunay-Star* (middle), *Hierarchical* (bottom).

size of 10). We use the Adam optimizer and the cross-entropy loss function with label smoothing (Szegedy et al., 2016) of 0.2. As data augmentation, we employ node dropping ($p = 0.1$), where nodes are dropped randomly from the adjacency matrix with probability p using samples from a Bernoulli distribution. For the experimental setups, where the coordinates are used as node labels, we additionally add random shearing (shearing factor range $[-1.05, 1.05]$), scaling ($\pm 5\%$), and random rotation (0 – 360°) of the coordinates, before zero centering. For the coordinate augmentation, we use the transform implementations provided by the PyG library.

The design choices are made based on previous empirical experience (Studer et al., 2021b), the original publications of the MP functions, and suggestions provided by (You et al., 2020), and validated on a preliminary dataset. GraphNorm and a low learning rate increase the training stability and show a more stable loss convergence on the validation sets. Data augmentation, dropout, loss smoothing, and weight decay help with overfit-

ting, as the dataset is small and unbalanced. The number of neurons is optimized between [128, 196, 256]. (You et al., 2020) suggest using the Adam optimizer, 4 MP layers, concatenation for JK, and sum aggregation for read-out (global-add pooling) work best.

Table 5: Overview of the 5-fold cross-validation split. Overall, there are 626 graphs from 575 patients, as multiple slides are available for some patients. For each slide, one hotspot is annotated from which a graph is extracted.

CV fold	# patients		# graphs	
	low-risk	high-risk	low-risk	high-risk
0	104	10	109	12
1	103	12	107	14
2	102	13	109	18
3	103	13	109	19
4	101	14	107	22
total	513	62	541	85

Table 6: Overview of the number of parameters in the different GNN configurations. The number depends on the message-passing (MP) function, the number of node/edge features, and whether or not Jumping Knowledge (JK) is used. The number of neurons and number of layers is kept fixed otherwise. Using the additional clinical data adds another 1,920 parameters to the respective model.

Node Features					
	Type	Type	Type	Type	
		Coord.	ViT-16	Coord.	ViT-16
# Node Features	2	2+2	2+384	2+2+384	
GATv2	-	375,938	376,706	523,394	524,162
	JK	2,590,466	2,591,234	2,737,922	2,738,690
GIN	-	411,650	412,034	485,378	485,762
	JK	2,626,946	2,627,330	2,700,674	2,701,058
GraphSAGE	-	372,866	373,634	520,322	521,090
	JK	2,588,162	2,588,930	2,735,618	2,736,386

Appendix E. Full Experimental Results

In this section, we present the full results for all experimental set-ups, with the per-class F1Score and precision in addition to the per-class recall. The results considered best and presented in Table 2 are highlighted in bold.

Table 7, 10, 13, and 16 show the results for the *Delaunay* graph representation with type, type + coordinates, type + ViT-16, and type + coordinates + ViT-16, respectively.

Table 8, 11, 14, and 17 show the results for the *Delaunay-Star* graph representation with type, type + coordinates, type + ViT-16, and type + coordinates + ViT-16, respectively.

Table 9, 12, 15, and 18 show the results for the *Hierarchical* graph representation with type, type + coordinates, type + ViT-16, and type + coordinates + ViT-16, respectively.

Table 7: Full results and additional metrics of experiments on the *Delaunay* graph representations using just the node type as a node label.

GNN	Clin. Info	F1Score Low-risk	F1Score High-risk	Precision Low-risk	Precision High-risk	Recall Low-risk (TNR)	Recall High-risk (TPR)
GATv2	No	23.8 ± 27.7	22.0 ± 4.4	58.3 ± 47.6	12.6 ± 3.0	16.9 ± 20.1	94.2 ± 8.4
	Yes	14.2 ± 17.5	19.9 ± 2.8	56.1 ± 46.0	11.2 ± 1.9	8.9 ± 11.4	94.1 ± 7.3
GATv2-JK	No	55.1 ± 10.7	23.5 ± 2.8	94.3 ± 2.5	13.9 ± 2.0	39.8 ± 10.9	79.6 ± 11.8
	Yes	54.9 ± 10.1	23.1 ± 1.7	94.9 ± 4.0	13.6 ± 0.9	39.6 ± 9.6	79.6 ± 15.3
GIN	No	48.6 ± 10.3	23.0 ± 3.0	94.9 ± 1.9	13.4 ± 2.1	33.4 ± 9.4	84.4 ± 9.1
	Yes	39.3 ± 16.8	21.9 ± 3.7	94.2 ± 3.6	12.6 ± 2.5	26.4 ± 13.8	86.0 ± 10.8
GIN-JK	No	57.4 ± 5.9	24.6 ± 3.2	95.1 ± 1.3	14.5 ± 2.2	41.3 ± 6.1	81.9 ± 7.3
	Yes	53.6 ± 3.0	22.7 ± 2.8	93.7 ± 1.1	13.3 ± 1.8	37.6 ± 2.9	78.7 ± 5.2
GraphSAGE	No	41.3 ± 8.1	22.7 ± 3.6	96.2 ± 3.2	13.1 ± 2.4	26.8 ± 7.1	90.1 ± 8.3
	Yes	32.9 ± 22.2	22.2 ± 2.9	77.8 ± 39.0	12.7 ± 2.1	22.2 ± 16.8	91.7 ± 10.2
GraphSAGE-JK	No	43.5 ± 4.5	22.7 ± 3.2	95.4 ± 1.4	13.0 ± 2.0	28.3 ± 3.8	88.4 ± 4.9
	Yes	47.1 ± 5.6	23.4 ± 3.0	95.7 ± 1.9	13.5 ± 1.9	31.4 ± 4.7	88.3 ± 5.1

Table 8: Full results and additional metrics of experiments on the *Delaunay-Star* graph representations using just the node type as a node label.

GNN	Clin. Info	F1Score Low-risk	F1Score High-risk	Precision Low-risk	Precision High-risk	Recall Low-risk (TNR)	Recall High-risk (TPR)
GATv2	No	43.7 ± 24.1	19.4 ± 1.8	87.2 ± 8.3	11.5 ± 1.6	32.6 ± 21.8	71.3 ± 20.6
	Yes	23.8 ± 5.4	18.7 ± 2.1	86.6 ± 8.6	10.5 ± 1.2	13.8 ± 3.5	84.3 ± 7.3
GATv2-JK	No	60.4 ± 10.8	21.5 ± 5.5	91.9 ± 4.1	12.9 ± 3.4	46.0 ± 11.5	65.8 ± 17.9
	Yes	43.6 ± 25.8	20.4 ± 3.3	91.1 ± 5.3	12.3 ± 2.9	33.2 ± 24.4	72.2 ± 18.4
GIN	No	19.0 ± 22.5	19.4 ± 1.7	86.5 ± 18.7	11.0 ± 1.3	13.0 ± 17.6	87.9 ± 14.2
	Yes	28.6 ± 20.7	21.8 ± 3.6	95.6 ± 6.5	12.5 ± 2.5	19.0 ± 16.8	92.5 ± 9.6
GIN-JK	No	68.5 ± 9.1	24.2 ± 6.0	92.3 ± 2.7	15.2 ± 4.2	55.2 ± 11.2	63.0 ± 11.5
	Yes	59.2 ± 15.9	22.5 ± 7.2	91.6 ± 4.2	13.6 ± 4.7	45.4 ± 15.0	68.1 ± 17.7
GraphSAGE	No	32.6 ± 18.7	19.9 ± 3.4	95.4 ± 5.8	11.4 ± 1.9	21.7 ± 14.5	84.0 ± 20.6
	Yes	50.7 ± 12.3	21.3 ± 2.0	93.9 ± 4.0	12.5 ± 1.1	36.1 ± 11.5	76.1 ± 16.9
GraphSAGE-JK	No	56.3 ± 11.9	22.9 ± 3.4	92.5 ± 1.9	13.6 ± 2.4	41.4 ± 12.1	73.9 ± 3.7
	Yes	55.0 ± 14.3	24.0 ± 4.8	95.1 ± 3.2	14.2 ± 3.2	40.2 ± 13.1	79.9 ± 13.5

Table 9: Full results and additional metrics of experiments on the *Hierarchical* graph representations using just the node type as a node label.

GNN	Clin. Info	F1 Score (%)		Precision (%)		Recall (%)	
		Low-risk	High-risk	Low-risk	High-risk	Low-risk (TNR)	High-risk (TPR)
GATv2	No	54.2 ± 22.3	20.9 ± 3.2	92.6 ± 4.0	12.9 ± 2.4	42.7 ± 23.3	68.5 ± 23.9
	Yes	37.0 ± 26.9	18.8 ± 6.9	70.6 ± 35.6	11.0 ± 4.4	27.5 ± 22.4	72.4 ± 26.8
GATv2-JK	No	34.4 ± 18.3	18.5 ± 3.6	89.0 ± 10.0	10.6 ± 2.2	23.0 ± 13.8	75.7 ± 18.4
	Yes	37.7 ± 6.9	17.1 ± 3.1	86.7 ± 6.2	9.8 ± 1.8	24.4 ± 5.6	68.9 ± 15.0
GIN	No	2.3 ± 2.2	19.0 ± 1.4	50.0 ± 44.7	10.6 ± 0.8	1.2 ± 1.1	97.1 ± 5.7
	Yes	1.8 ± 3.7	19.6 ± 1.6	20.0 ± 40.0	10.9 ± 1.0	1.0 ± 1.9	100.0 ± 0.0
GIN-JK	No	38.8 ± 25.6	22.1 ± 4.7	91.4 ± 11.1	12.9 ± 3.4	27.9 ± 20.7	83.7 ± 13.5
	Yes	48.4 ± 20.5	21.2 ± 4.7	88.9 ± 8.3	12.6 ± 3.1	35.4 ± 17.4	73.6 ± 15.3
GraphSAGE	No	36.0 ± 20.7	21.1 ± 3.3	94.2 ± 3.3	12.2 ± 2.2	24.8 ± 17.7	84.7 ± 16.1
	Yes	46.0 ± 22.3	22.5 ± 5.2	91.9 ± 3.3	13.3 ± 3.8	33.6 ± 19.6	78.9 ± 10.7
GraphSAGE-JK	No	51.2 ± 16.1	21.6 ± 4.0	92.9 ± 4.4	12.8 ± 2.6	37.2 ± 15.3	74.3 ± 16.0
	Yes	63.7 ± 4.7	23.7 ± 4.0	93.6 ± 3.2	14.3 ± 2.6	48.6 ± 6.1	71.5 ± 14.8

Table 10: Full results and additional metrics of experiments on the *Delaunay* graph representations using the node type and the coordinates as a node label.

GNN	Clin. Info	F1 Score (%)		Precision (%)		Recall (%)	
		Low-risk	High-risk	Low-risk	High-risk	Low-risk (TNR)	High-risk (TPR)
GATv2	No	13.7 ± 7.3	19.5 ± 2.4	91.0 ± 7.6	10.9 ± 1.4	7.6 ± 4.4	93.5 ± 5.9
	Yes	22.7 ± 13.7	20.1 ± 2.8	73.0 ± 36.7	11.3 ± 1.8	13.7 ± 8.7	90.4 ± 5.7
GATv2-JK	No	29.8 ± 21.8	17.4 ± 3.7	86.6 ± 11.7	9.9 ± 2.0	20.5 ± 16.7	75.9 ± 25.7
	Yes	26.0 ± 16.4	19.9 ± 1.4	93.9 ± 5.3	11.3 ± 1.0	16.4 ± 11.9	88.1 ± 13.2
GIN	No	18.2 ± 12.0	19.8 ± 1.5	95.0 ± 6.1	11.1 ± 1.0	10.8 ± 8.5	92.7 ± 11.1
	Yes	16.2 ± 6.2	20.4 ± 2.7	97.1 ± 5.7	11.4 ± 1.7	9.0 ± 3.7	96.7 ± 6.7
GIN-JK	No	34.0 ± 22.4	20.3 ± 1.9	95.2 ± 4.3	11.8 ± 1.6	24.1 ± 21.1	83.0 ± 21.4
	Yes	27.9 ± 18.5	19.2 ± 3.1	89.3 ± 6.9	11.0 ± 2.0	18.2 ± 13.8	82.2 ± 13.4
GraphSAGE	No	19.1 ± 12.8	19.3 ± 2.2	89.4 ± 6.7	10.9 ± 1.4	11.3 ± 8.4	89.1 ± 7.2
	Yes	16.5 ± 7.9	18.9 ± 2.5	90.7 ± 7.8	10.6 ± 1.5	9.4 ± 4.9	88.6 ± 9.5
GraphSAGE-JK	No	21.2 ± 13.8	20.5 ± 2.8	95.8 ± 3.6	11.6 ± 1.8	12.7 ± 9.3	93.6 ± 5.6
	Yes	25.1 ± 12.8	17.3 ± 3.4	87.9 ± 8.5	9.8 ± 1.8	15.6 ± 9.7	78.5 ± 22.5

Table 11: Full results and additional metrics of experiments on the *Delaunay-Star* graph representations using the node type and the coordinates as a node label.

GNN	Clin. Info	F1 Score (%)		Precision (%)		Recall (%)	
		Low-risk	High-risk	Low-risk	High-risk	Low-risk (TNR)	High-risk (TPR)
GATv2	No	19.5 ± 9.2	18.9 ± 2.2	88.3 ± 6.0	10.6 ± 1.3	11.3 ± 6.2	87.2 ± 10.2
	Yes	17.7 ± 6.6	19.1 ± 3.2	86.4 ± 16.8	10.7 ± 1.9	9.9 ± 4.0	89.3 ± 13.1
GATv2-JK	No	49.4 ± 7.8	21.6 ± 2.9	94.1 ± 4.2	12.6 ± 1.7	34.1 ± 7.5	79.2 ± 15.8
	Yes	38.0 ± 5.6	21.4 ± 2.0	93.8 ± 1.9	12.2 ± 1.3	24.0 ± 4.6	87.3 ± 2.9
GIN	No	21.7 ± 26.6	20.5 ± 3.3	56.6 ± 46.3	11.7 ± 2.4	15.5 ± 19.7	89.7 ± 12.8
	Yes	14.8 ± 23.5	18.8 ± 1.4	52.8 ± 43.8	10.6 ± 0.9	10.7 ± 18.1	87.9 ± 17.9
GIN-JK	No	35.7 ± 25.0	20.6 ± 2.6	94.9 ± 4.5	12.0 ± 1.9	25.5 ± 19.2	82.2 ± 16.9
	Yes	45.8 ± 31.7	23.2 ± 6.2	92.4 ± 5.7	14.2 ± 4.7	36.7 ± 27.6	77.1 ± 18.4
GraphSAGE	No	45.1 ± 9.3	21.8 ± 3.7	93.2 ± 3.1	12.6 ± 2.4	30.2 ± 8.0	82.4 ± 8.7
	Yes	42.1 ± 8.6	19.9 ± 3.7	91.4 ± 3.8	11.5 ± 2.2	27.9 ± 7.5	76.9 ± 12.9
GraphSAGE-JK	No	54.6 ± 7.1	22.9 ± 4.9	93.1 ± 2.8	13.5 ± 3.1	38.8 ± 6.7	77.0 ± 6.7
	Yes	51.4 ± 9.1	22.9 ± 4.4	93.5 ± 2.3	13.4 ± 2.9	35.9 ± 8.2	80.2 ± 5.6

Table 12: Full results and additional metrics of experiments on the *Hierarchical* graph representations using the node type and the coordinates as a node label.

GNN	Clin. Info	F1 Score (%)		Precision (%)		Recall (%)	
		Low-risk	High-risk	Low-risk	High-risk	Low-risk (TNR)	High-risk (TPR)
GATv2	No	26.7 ± 12.1	20.5 ± 2.0	95.4 ± 4.4	11.6 ± 1.3	16.3 ± 8.4	91.2 ± 10.5
	Yes	22.8 ± 7.4	19.2 ± 1.7	92.2 ± 7.3	10.8 ± 1.0	13.3 ± 5.0	88.0 ± 11.8
GATv2-JK	No	40.4 ± 3.3	20.3 ± 3.2	91.9 ± 3.6	11.6 ± 2.0	26.0 ± 2.8	80.5 ± 9.7
	Yes	39.3 ± 17.8	21.7 ± 3.4	95.7 ± 4.7	12.5 ± 2.2	26.5 ± 13.9	86.0 ± 14.9
GIN	No	0.4 ± 0.8	19.2 ± 1.9	20.0 ± 40.0	10.6 ± 1.1	0.2 ± 0.4	98.5 ± 3.1
	Yes	0.8 ± 1.0	19.5 ± 1.9	40.0 ± 49.0	10.8 ± 1.2	0.4 ± 0.5	100.0 ± 0.0
GIN-JK	No	19.2 ± 23.8	20.2 ± 4.0	80.9 ± 15.5	11.5 ± 2.8	13.4 ± 19.1	88.9 ± 7.8
	Yes	23.0 ± 17.1	19.7 ± 2.5	71.6 ± 36.0	11.1 ± 1.5	14.4 ± 11.5	88.1 ± 10.1
GraphSAGE	No	48.3 ± 16.9	22.1 ± 4.1	92.8 ± 1.2	13.0 ± 2.9	34.6 ± 15.8	77.8 ± 10.5
	Yes	44.9 ± 9.2	22.2 ± 4.1	95.0 ± 3.4	12.8 ± 2.5	30.0 ± 8.4	84.4 ± 14.3
GraphSAGE-JK	No	53.2 ± 9.6	23.0 ± 3.5	93.9 ± 2.0	13.6 ± 2.4	37.9 ± 9.6	79.3 ± 8.4
	Yes	57.0 ± 7.4	23.5 ± 3.2	94.0 ± 2.6	13.9 ± 2.1	41.4 ± 7.8	78.1 ± 11.6

Table 13: Full results and additional metrics of experiments on the *Delaunay* graph representations using the node type and the ViT-16 embedding as a node label.

GNN	Clin. Info	F1 Score (%)		Precision (%)		Recall (%)	
		Low-risk	High-risk	Low-risk	High-risk	Low-risk (TNR)	High-risk (TPR)
GATv2	No	51.2 ± 7.6	24.7 ± 6.1	95.8 ± 4.0	14.4 ± 3.8	35.1 ± 6.5	87.6 ± 11.4
	Yes	47.9 ± 11.6	24.7 ± 5.9	96.4 ± 3.9	14.4 ± 4.0	32.6 ± 10.8	90.5 ± 9.6
GATv2-JK	No	60.1 ± 8.1	24.1 ± 5.8	93.7 ± 2.3	14.5 ± 3.9	44.7 ± 8.7	75.3 ± 10.3
	Yes	57.7 ± 8.7	24.3 ± 5.7	94.2 ± 2.4	14.5 ± 3.8	42.2 ± 8.8	78.3 ± 9.6
GIN	No	53.1 ± 9.1	22.8 ± 5.4	93.6 ± 2.7	13.4 ± 3.4	37.7 ± 8.8	78.1 ± 12.3
	Yes	51.7 ± 2.7	24.2 ± 2.6	95.8 ± 1.2	14.1 ± 1.7	35.5 ± 2.6	87.2 ± 3.4
GIN-JK	No	68.1 ± 4.7	25.6 ± 5.4	93.9 ± 1.5	15.7 ± 3.7	53.6 ± 5.8	70.5 ± 10.7
	Yes	67.1 ± 6.1	25.0 ± 3.6	93.6 ± 1.4	15.4 ± 2.7	52.7 ± 7.4	69.9 ± 7.3
GraphSAGE	No	63.5 ± 7.8	25.1 ± 4.7	93.9 ± 0.6	15.2 ± 3.4	48.5 ± 9.2	73.9 ± 3.7
	Yes	58.7 ± 10.1	22.4 ± 6.0	91.7 ± 2.5	13.5 ± 4.0	43.7 ± 10.1	68.7 ± 6.0
GraphSAGE-JK	No	64.0 ± 12.8	27.7 ± 8.0	94.8 ± 1.7	17.1 ± 5.8	49.6 ± 14.2	78.5 ± 5.9
	Yes	65.1 ± 5.6	25.0 ± 6.3	93.7 ± 1.8	15.3 ± 4.4	50.1 ± 6.3	72.0 ± 9.1

Table 14: Full results and additional metrics of experiments on the *Delaunay-Star* graph representations using the node type and the ViT-16 embedding as a node label.

GNN	Clin. Info	F1 Score (%)		Precision (%)		Recall (%)	
		Low-risk	High-risk	Low-risk	High-risk	Low-risk (TNR)	High-risk (TPR)
GATv2	No	42.9 ± 8.1	20.8 ± 5.2	92.1 ± 4.2	12.0 ± 3.1	28.3 ± 6.3	79.3 ± 13.5
	Yes	51.4 ± 9.0	21.6 ± 4.6	92.2 ± 2.6	12.7 ± 3.0	36.1 ± 8.4	75.2 ± 8.2
GATv2-JK	No	61.6 ± 6.6	23.8 ± 7.2	93.0 ± 3.0	14.4 ± 4.8	46.2 ± 6.8	71.6 ± 11.7
	Yes	63.9 ± 12.3	27.6 ± 8.9	94.4 ± 3.2	17.0 ± 6.2	49.2 ± 13.1	78.3 ± 8.2
GIN	No	37.1 ± 27.0	23.4 ± 7.6	91.4 ± 3.6	14.0 ± 5.6	27.3 ± 23.9	85.9 ± 6.7
	Yes	45.8 ± 27.6	24.0 ± 5.7	95.1 ± 2.6	14.3 ± 4.1	34.7 ± 23.0	82.9 ± 10.8
GIN-JK	No	59.0 ± 21.6	26.4 ± 9.3	92.5 ± 3.9	16.4 ± 6.9	46.3 ± 20.9	75.2 ± 9.3
	Yes	55.3 ± 19.4	26.5 ± 7.0	95.0 ± 2.0	16.0 ± 5.0	41.5 ± 18.6	84.2 ± 6.1
GraphSAGE	No	58.1 ± 9.6	25.6 ± 7.8	94.6 ± 3.6	15.3 ± 5.3	42.4 ± 9.8	81.3 ± 11.0
	Yes	59.4 ± 9.6	24.8 ± 8.2	94.0 ± 4.1	14.9 ± 5.5	44.1 ± 10.6	76.6 ± 16.5
GraphSAGE-JK	No	63.4 ± 7.6	25.5 ± 6.8	94.0 ± 2.6	15.5 ± 4.6	48.2 ± 8.1	75.1 ± 9.5
	Yes	66.7 ± 6.5	27.1 ± 6.1	94.9 ± 1.6	16.6 ± 4.1	51.7 ± 7.2	76.8 ± 7.6

Table 15: Full results and additional metrics of experiments on the *Hierarchical* graph representations using the node type and the ViT-16 embedding as a node label.

GNN	Clin. Info	F1 Score (%)		Precision (%)		Recall (%)	
		Low-risk	High-risk	Low-risk	High-risk	Low-risk (TNR)	High-risk (TPR)
GATv2	No	44.4 ± 11.2	22.7 ± 6.1	93.9 ± 4.5	13.2 ± 4.0	29.7 ± 10.2	85.0 ± 9.8
	Yes	55.5 ± 15.7	26.8 ± 10.0	94.7 ± 3.6	16.2 ± 6.9	40.7 ± 15.6	84.8 ± 8.4
GATv2-JK	No	57.1 ± 7.0	23.6 ± 5.5	93.6 ± 2.2	14.0 ± 3.6	41.4 ± 7.1	76.8 ± 7.6
	Yes	58.4 ± 8.6	23.0 ± 6.7	92.6 ± 3.8	13.8 ± 4.4	43.2 ± 8.8	72.4 ± 12.4
GIN	No	5.5 ± 6.0	19.3 ± 1.3	56.0 ± 46.3	10.7 ± 0.8	2.9 ± 3.3	97.1 ± 5.7
	Yes	5.4 ± 7.1	19.7 ± 2.2	80.0 ± 40.0	10.9 ± 1.3	2.9 ± 3.9	98.5 ± 3.1
GIN-JK	No	59.3 ± 3.5	22.2 ± 5.0	92.6 ± 2.1	13.2 ± 3.2	43.7 ± 3.7	70.0 ± 10.3
	Yes	57.2 ± 13.7	23.3 ± 5.4	92.8 ± 4.6	14.0 ± 3.6	42.6 ± 14.2	73.5 ± 13.3
GraphSAGE	No	63.6 ± 6.9	25.0 ± 7.1	93.8 ± 3.2	15.1 ± 4.6	48.4 ± 7.2	73.6 ± 13.3
	Yes	58.8 ± 9.1	25.2 ± 6.5	94.4 ± 2.6	15.0 ± 4.3	43.1 ± 8.8	79.9 ± 8.0
GraphSAGE-JK	No	61.9 ± 11.7	25.1 ± 7.1	93.3 ± 2.7	15.3 ± 4.8	47.3 ± 12.2	73.7 ± 6.9
	Yes	61.0 ± 9.8	25.8 ± 7.1	94.4 ± 2.3	15.5 ± 4.8	45.7 ± 10.3	78.3 ± 7.7

Table 16: Full results and additional metrics of experiments on the *Delaunay* graph representations using the node type, the coordinates and the ViT-16 embedding as a node label.

GNN	Clin. Info	F1 Score (%)		Precision (%)		Recall (%)	
		Low-risk	High-risk	Low-risk	High-risk	Low-risk (TNR)	High-risk (TPR)
GATv2	No	24.5 ± 11.3	19.8 ± 2.2	89.7 ± 8.2	11.2 ± 1.4	14.7 ± 7.5	88.8 ± 7.4
	Yes	33.1 ± 13.4	20.4 ± 3.4	90.6 ± 3.4	11.7 ± 2.3	21.1 ± 11.1	84.2 ± 3.6
GATv2-JK	No	49.2 ± 15.7	22.2 ± 6.2	91.5 ± 4.0	13.1 ± 4.2	34.9 ± 14.0	76.8 ± 7.6
	Yes	46.9 ± 16.1	22.9 ± 6.0	92.7 ± 3.0	13.4 ± 4.1	32.8 ± 14.5	81.7 ± 5.9
GIN	No	36.6 ± 4.5	21.5 ± 2.6	94.3 ± 1.8	12.2 ± 1.6	22.8 ± 3.4	88.7 ± 3.6
	Yes	30.6 ± 10.0	20.7 ± 3.1	92.1 ± 5.1	11.8 ± 2.0	18.8 ± 7.4	88.7 ± 3.6
GIN-JK	No	47.0 ± 15.5	23.4 ± 6.4	93.9 ± 4.1	13.8 ± 4.4	32.9 ± 14.9	83.3 ± 9.8
	Yes	45.0 ± 11.1	21.5 ± 4.1	92.5 ± 1.3	12.5 ± 2.7	30.5 ± 10.0	80.2 ± 5.6
GraphSAGE	No	38.1 ± 5.6	21.4 ± 3.6	93.6 ± 2.6	12.2 ± 2.3	24.0 ± 4.3	86.6 ± 5.1
	Yes	51.6 ± 14.4	24.3 ± 9.6	92.9 ± 4.5	14.6 ± 6.7	37.0 ± 14.8	80.2 ± 11.0
GraphSAGE-JK	No	47.1 ± 15.1	21.7 ± 6.7	90.5 ± 4.3	12.8 ± 4.6	33.1 ± 14.4	75.4 ± 6.4
	Yes	47.9 ± 14.7	22.8 ± 5.7	92.6 ± 3.3	13.5 ± 4.1	33.6 ± 14.2	80.6 ± 3.7

Table 17: Full results and additional metrics of experiments on the *Delaunay-Star* graph representations using the node type, the coordinates and the ViT-16 embedding as a node label.

GNN	Clin. Info	F1 Score (%)		Precision (%)		Recall (%)	
		Low-risk	High-risk	Low-risk	High-risk	Low-risk (TNR)	High-risk (TPR)
GATv2	No	33.3 ± 16.7	21.2 ± 2.6	95.2 ± 3.9	12.1 ± 1.9	21.8 ± 13.4	88.1 ± 10.8
	Yes	31.7 ± 6.5	20.7 ± 3.0	93.3 ± 1.9	11.8 ± 1.9	19.3 ± 4.6	88.3 ± 5.1
GATv2-JK	No	49.5 ± 12.2	23.4 ± 5.8	93.8 ± 2.5	13.8 ± 4.0	34.6 ± 12.0	82.5 ± 5.6
	Yes	50.1 ± 12.3	22.9 ± 3.6	94.3 ± 3.4	13.4 ± 2.5	35.2 ± 11.3	81.6 ± 10.3
GIN	No	18.7 ± 23.7	20.9 ± 3.5	57.3 ± 46.9	11.8 ± 2.4	12.7 ± 16.9	93.8 ± 7.5
	Yes	4.5 ± 2.5	19.8 ± 1.8	80.0 ± 40.0	11.0 ± 1.1	2.3 ± 1.3	100.0 ± 0.0
GIN-JK	No	51.6 ± 24.2	21.8 ± 5.0	88.1 ± 8.4	13.2 ± 3.8	39.7 ± 21.4	70.1 ± 10.7
	Yes	47.4 ± 20.6	23.9 ± 4.9	95.3 ± 3.1	14.2 ± 3.5	34.4 ± 18.8	84.5 ± 10.4
GraphSAGE	No	43.5 ± 9.5	22.5 ± 4.1	94.7 ± 4.1	13.0 ± 2.5	28.7 ± 7.8	86.9 ± 10.9
	Yes	44.0 ± 5.4	22.8 ± 4.0	95.2 ± 2.2	13.1 ± 2.5	28.7 ± 4.3	88.2 ± 5.4
GraphSAGE-JK	No	53.5 ± 9.1	23.6 ± 5.7	93.8 ± 2.0	13.9 ± 3.8	37.9 ± 8.9	80.1 ± 5.9
	Yes	54.7 ± 5.0	24.7 ± 3.7	95.7 ± 2.9	14.5 ± 2.3	38.4 ± 4.8	85.7 ± 9.9

Table 18: Full results and additional metrics of experiments on the *Hierarchical* graph representations using the node type, the coordinates and the ViT-16 embedding as a node label.

GNN	Clin. Info	F1 Score (%)		Precision (%)		Recall (%)	
		Low-risk	High-risk	Low-risk	High-risk	Low-risk (TNR)	High-risk (TPR)
GATv2	No	25.9 ± 8.1	21.0 ± 3.3	94.7 ± 7.2	11.8 ± 2.0	15.3 ± 5.5	93.6 ± 7.9
	Yes	27.2 ± 12.9	21.3 ± 2.7	96.2 ± 5.2	12.0 ± 1.7	16.6 ± 9.3	93.8 ± 7.5
GATv2-JK	No	45.5 ± 14.3	22.0 ± 4.4	91.8 ± 3.6	12.8 ± 2.8	31.2 ± 11.7	80.7 ± 2.9
	Yes	48.6 ± 16.2	22.5 ± 4.4	92.3 ± 3.6	13.2 ± 3.0	34.4 ± 14.0	79.4 ± 6.7
GIN	No	1.2 ± 0.9	19.5 ± 1.9	60.0 ± 49.0	10.8 ± 1.1	0.6 ± 0.5	100.0 ± 0.0
	Yes	0.4 ± 0.8	19.5 ± 1.8	20.0 ± 40.0	10.8 ± 1.1	0.2 ± 0.4	100.0 ± 0.0
GIN-JK	No	34.1 ± 22.2	21.4 ± 4.1	93.8 ± 4.0	12.4 ± 2.8	23.4 ± 17.9	85.5 ± 10.5
	Yes	43.2 ± 21.1	22.3 ± 4.8	92.2 ± 3.4	13.2 ± 3.5	30.9 ± 19.2	81.3 ± 9.4
GraphSAGE	No	38.0 ± 15.2	21.9 ± 5.0	91.3 ± 7.2	12.6 ± 3.2	24.8 ± 11.1	86.6 ± 5.1
	Yes	48.3 ± 17.2	23.3 ± 3.7	95.7 ± 2.7	13.6 ± 2.6	34.2 ± 14.3	84.0 ± 10.9
GraphSAGE-JK	No	57.6 ± 16.7	26.3 ± 7.1	94.2 ± 5.0	15.9 ± 4.8	43.2 ± 15.9	81.9 ± 11.4
	Yes	58.3 ± 8.3	25.6 ± 3.3	95.8 ± 1.5	15.2 ± 2.3	42.5 ± 8.9	84.0 ± 8.2

